

Charge Transfer and dd excitations in AgF_2

Nimrod Bachar,^{1,*} Kacper Koterwas,² Jakub Gawraczynski,² Waldemar Trzcinski,³ Józef Paszula,³ Riccardo Piombo,⁴ Paolo Barone,⁵ Zoran Mazej,⁶ Giacomo Ghiringhelli,^{7,8} Abhishek Nag,⁹ Ke-Jin Zhou,⁹ José Lorenzana,^{10,†} Dirk van der Marel,¹ and Wojciech Grochala²

¹*Department of Quantum Matter Physics, University of Geneva, CH-1211 Geneva 4, Switzerland*

²*Center of New Technologies, University of Warsaw, Żwirki i Wigury 93, 02-089 Warsaw, Poland*

³*Department of New Technologies and Chemistry, Military University of Technology, gen. Sylwestra Kaliskiego 2, 00-908 Warsaw, Poland*

⁴*Dipartimento di Fisica, Università di Roma "La Sapienza", 00185 Rome, Italy*

⁵*Superconducting and Other Innovative Materials and Devices Institute (SPIN), Consiglio Nazionale delle Ricerche, Area della Ricerca di Tor Vergata, Via del Fosso del Cavaliere 100, I-00133 Rome, Italy*

⁶*Department of Inorganic Chemistry and Technology, Jožef Stefan Institute, Jamova cesta 39, 1000 Ljubljana, Slovenia*

⁷*Dipartimento di Fisica, Politecnico di Milano, piazza Leonardo da Vinci 32, 20133 Milano, Italy*

⁸*CNR-SPIN, Dipartimento di Fisica, Politecnico di Milano, piazza Leonardo da Vinci 32, 20133 Milano, Italy*

⁹*Diamond Light Source, Harwell Campus, Didcot OX11 0DE, United Kingdom*

¹⁰*Institute for Complex Systems (ISC), Consiglio Nazionale delle Ricerche, Dipartimento di Fisica, Università di Roma "La Sapienza", 00185 Rome, Italy*

Charge transfer (CT) insulators are the parent phase of a large group of today's unconventional high temperature superconductors. Here we study experimentally and theoretically the interband excitations of the CT insulator silver fluoride AgF_2 , which has been proposed as an excellent analogue of oxocuprates. Optical conductivity and resonant inelastic x-ray scattering (RIXS) on AgF_2 polycrystalline sample show a close similarity with that measured on undoped La_2CuO_4 . While the former shows a CT gap ~ 3.4 eV, larger than in the cuprate, dd -excitations are nearly at the same energy in the two materials. DFT and exact diagonalization cluster computations of the multiplet spectra show that AgF_2 is more covalent than the cuprate, in spite of the larger fundamental gap. Furthermore, we show that AgF_2 is at the verge of a charge transfer instability. The overall resemblance of our data on AgF_2 to those published previously on La_2CuO_4 suggests that the underlying CT insulator physics is the same, while AgF_2 could also benefit from a proximity to a charge density wave phase as in BaBiO_3 . Therefore, our work provides a compelling support to the future use of fluoroargentates for materials' engineering of novel high-temperature superconductors.

I. INTRODUCTION

Following the discovery of a high- T_c superconductivity in the cuprate oxide (CuO) family, there has been an ongoing search for other systems in which it will be possible to replicate such novel properties. Apart from purely fundamental research into the underlying physics of the unconventional superconducting state, there has also been the goal to find T_c at higher temperatures.

In most cases, the key players of this approach were elements originating - like copper - from the transition metal group of the periodic table, and over time several candidates came into focus such as iridates, nickelates, and vanadates. The vanadates^{1,2} appear to be extremely resilient to external doping³ unlike the various compounds of the cuprate family. Superconductivity under doping was predicted theoretically in iridates⁴, which are isostructural to the cuprates and share several similarities with the properties of the antiferromagnetic (AFM) phase. However, there are some distinct differences compared to the cuprates. First, there is a strong competition between electronic correlations, spin-orbit coupling, and crystal field energy scales in the iridates. Second, Sr_2IrO_4 is a Mott insulator⁵, while La_2CuO_4

is a Charge Transfer (CT) insulator. Extensive experimental studies via various doping approaches did not result in any signatures for superconducting properties even upon heavy doping levels, as in the $\text{La}_{2-x}\text{Sr}_x\text{IrO}_4$ compound⁵⁻⁷. Quite interestingly, although NdNiO_3 has neither the AFM ground state nor the strong covalent bonding commonly found in cuprates, Sr doped NdNiO_2 exhibits low temperature superconductivity in an infinite layer structure as was shown recently⁸.

There is, however, another approach to replace copper, and that is by staying in the same column of the periodic table of elements and by choosing silver. It was already clear from the early stages of that paradigm that silver oxide cannot become a true charge transfer insulator because of the high second ionization energy of silver and the fact that oxygen is not a sufficiently electronegative element⁹. As a result, AgO has a negative charge transfer energy that ends up in the Ag^{1+} oxidation state without a magnetic ordering as opposed to its sibling, CuO . Fluorine is more electronegative than oxygen, therefore has deeper $2p^6$ states, which results in a positive charge transfer energy. Several fluoroargentates were found to be iso-electronic to their cuprate sibling La_2CuO_4 . However, previous work showed that their magnetic ground state

is not the same as, for example, in the case of Cs_2AgF_4 ¹⁰ and K_2AgF_4 , both being ferromagnetic¹¹, with small local structural distortions of the AgF_6 octahedron stabilizing an antiferro orbital ordering.¹²

Recent calculations predict that the magnetic ground state of KAgF_3 and AgF_2 is AFM. KAgF_3 has an arrangement of spins within the zig-zag chain along the crystallographic c-axis direction forming an AFM with a low temperature Néel transition and a theoretical gap of 0.7 eV^{11,13}. However, its quasi-1D magnetic structure cannot be compared directly with the quasi-2D AFM state of the cuprates. On the other hand, AgF_2 has a neutral-plane stacked structure due to the inherent F^- character (instead of O^{2-} in CuO_2), although with strongly buckled planes. Therefore, AgF_2 is the "012" equivalent (free of charge reservoir layer) of the 214 stoichiometry in cuprates^{11,14}. The Néel temperature of AgF_2 ($T_N = 163$ K) is half of that for La_2CuO_4 ($T_N = 325$ K). LSDA+U calculations predicted a gap of 1.5 eV to 2.5 eV in various forms of AgF_2 ¹⁵⁻¹⁷. Hybrid DFT calculations involving orbital character confirmed the striking resemblance of the electronic structure of AgF_2 and its cuprate analog La_2CuO_4 ¹⁴. Furthermore it predicted also the exchange energy J to be about 70 meV in AgF_2 ^{14,17}, half of the J value in typical cuprate compounds. A one-to-one comparison of the two-magnon excitation in Raman spectroscopy data of AgF_2 and $\text{EuBa}_2\text{Cu}_3\text{O}_6$ confirmed the expected J of about 70 meV in AgF_2 ¹⁴. Although the charge transfer gap between the F 2*p* state and the Ag 4*d* state was predicted by theoretical calculations, a direct experimental verification is still lacking^{11,14}.

In this work, we study the high energy excitations of AgF_2 by combining optical spectroscopy and resonant inelastic x-ray scattering (RIXS). The excitation spectrum is compared with cluster computation aided with DFT computation of parameters. We show that the optical conductivity spectrum close to the charge transfer gap resembles that of the oxocuprates. We also identify several *dd*-excitations in RIXS spectra. Our experimental observations are supported by the theoretical predictions of the electronic excitations in AgF_2 . The striking similarity between fluoroargentate and oxocuprates suggests that the former could be a promising candidate for a future high- T_c superconductor and a novel and interesting testbed for further investigations of electronic correlations in quantum materials.

II. METHODS

A. Sample preparation

A 10 g batch of polycrystalline AgF_2 has been freshly prepared as described previously¹⁴. Purity of the obtained sample has been verified using powder x-ray diffraction testifying to the presence of minute amounts (ca. 1 wt %) of diamagnetic AgF only.

To obtain a compact specimen of AgF_2 for optical measurements, an explosion compaction procedure was applied as described in Appendix A. Sample cylinder was cut into ca. 2 mm thin hard compact wafers which were fine polished inside the glovebox using diamond paper before performing any optical measurements.

Samples were loaded inside the cryostat chamber using an inert gas filled glove bag and with an active flow of gas, with a loading period of a few minutes, followed by evacuation of the sample chamber to ultra high vacuum (UHV). No visual changes of the sample surface could be seen, testifying the successful loading without any chemical deterioration of the sample.

B. Optical spectroscopy

The optical response of polished pressed powder AgF_2 samples was measured by combining infrared reflectivity and ellipsometry. The sample was installed in an UHV helium flow cryostat and data was recorded at selected temperatures from room temperature down to 8 K. The cryostat is designed to maintain a high position stability of the mounted sample during cooldown. Measurements were obtained using a near normal incident reflectivity setup in a Bruker Vertex 70V Fourier transform infrared (FTIR) spectrometer in the photon energy range of approximately 3.5 meV to 0.6 eV. Calibration spectra were obtained by measuring a gold layer deposited on top of the sample using in-situ thermal evaporation. In the photon energy range of 0.5 eV to 3.5 eV the complex dielectric function was determined using a Woollam VASE[®] spectroscopic ellipsometer. The ratios of the reflection coefficients for *p* and *s* polarized light $\rho = r_p/r_s$, were measured at incident angles of 61° and 63° (See Appendix B).

The optical conductivity was calculated directly from the pseudo-dielectric function using two sets of ellipsometry data at two different angles of incidence. In addition, we have fitted the ellipsometry parameters, Ψ_{ellip} and Δ_{ellip} to the Drude-Lorentz parametrization to obtain boundaries for our confidence in the optical conductivity spectra. We have used the far-IR reflectivity data to obtain the contribution of phonons to the spectra. The fit to the lowest energy phonon at about 30 cm^{-1} along with the fit to the ensemble of all far infrared (FIR) phonons were used to extrapolate the reflectivity to zero frequency. The frequency and temperature dependence of the real part of the optical conductivity will be discussed in section III.

C. RIXS

A polycrystalline sample was mounted on a copper sample holder in an inert atmosphere inside a glove box, loaded in a vacuum suitcase, and transferred to the experimental chamber maintained at $\approx 5 \times 10^{-10}$ mbar. The F K-edge x-ray absorption (XAS) spectrum was col-

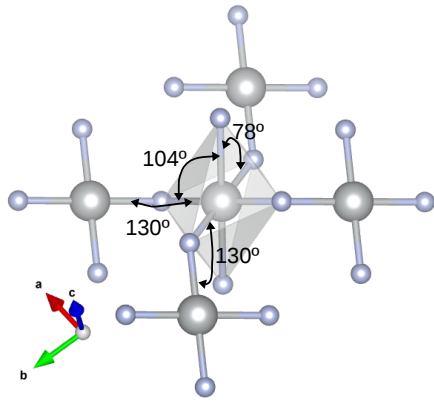


FIG. 1: The central grey octahedron shows the AgF_6 cluster used in the computations. The surrounding atoms are implicitly taken into account in the definition of diagonal energies. Some key bond angles are indicated for clarity.

lected in the fluorescence yield mode using σ -polarisation (normal to the scattering plane) at an angle of incidence of 75° . Resonant inelastic x-ray scattering (RIXS) spectra were collected at F K-edge with an energy resolution of $\delta E \approx 0.045$ eV at a scattering angle of 150° at 13 K, at I21-RIXS beam line, Diamond Light Source, United Kingdom¹⁸. The zero-energy transfer position and energy resolution of the RIXS spectra were determined from subsequent measurements of elastic peaks from an adjacent carbon tape. The RIXS spectrum was collected with π -polarisation (parallel to the scattering plane) at 682.2 eV at an angle of incidence of 20° for 30 min. The RIXS spectrum was fitted with Gaussian lineshapes for the elastic peak and phonons, with a damped harmonic oscillator model for the bimagnon, with Gaussian lineshapes for the dd -excitations and charge transfer excitation, and a fluorescence model¹⁹ for the emission feature peaking around 5 eV. The incident energy map was collected at an angle of incidence of 20° and σ -polarisation. RIXS spectra comparison after 6 hrs of x-ray beam exposure showed only a reduction in the overall emission signal, with no noticeable difference in the intensity ratios of the inelastic features (not shown).

D. Theory

To model the AgF_2 electronic excitations with Ag in a formally d^9 state, we considered an $(\text{AgF}_6)^{4-}$ cluster reproducing the local environment of the transition metal ion as shown in Fig. 1. The one-particle parameters were obtained from unpolarized DFT calculations of the periodic solid using the projector-augmented wave (PAW) method as implemented in VASP²⁰ within the generalized gradient approximation of Perdew, Burke, and Ernzerhof²¹ (PBE) using a mesh of $8 \times 8 \times 8$ k -points.

The band structure was obtained with the experimental lattice parameters of Ref. 22 and then projected onto maximally localized Wannier functions as implemented in the Wannier90 code²³. We used a Wannier basis with five d -orbitals per Ag and three p -orbitals per F. The two planar F-Ag-F bridges deviate slightly from orthogonality (93.3°). For the d -orbitals, we took the axes so that the bisectrix of the axes coincides with the bisectrix of the bridges, resulting in axes nearly oriented along AgF bonds. For the p -orbitals we used the local reference frame as in Ref. 14.

The Wannier90 one-particle Hamiltonian for the solid was truncated to the AgF_6 cluster yielding a Hamiltonian with 5 d -orbitals and $3 \times 6 = 18$ p -orbitals. The one-particle Hamiltonian reads

$$\begin{aligned}
 H_{pd} = & \sum_{\nu} \varepsilon_d(\nu) d_{\nu}^{\dagger} d_{\nu} + \sum_m \varepsilon_p(m) p_m^{\dagger} p_m \\
 & + \sum_{\nu m} t_{pd}(\nu, m) d_{\nu}^{\dagger} p_m + h.c. \\
 & + \sum_{mm'} t_{pp}(m, m') p_m^{\dagger} p_{m'} + h.c., \quad (1)
 \end{aligned}$$

where ν, m are spin-orbital indexes, d_{ν}^{\dagger} creates a hole in the d -orbitals ($d_{3z^2-r^2}$, $d_{x^2-y^2}$, d_{xy} , d_{xz} , d_{yz}) while p_m^{\dagger} creates a hole in one of the 18 p -orbitals. We considered pd hopping across the 6 F-Ag bonds [$t_{pd}(\nu, m)$] and pp hopping across the 12 F-F bonds forming the edges of the octahedral cage [$t_{pp}(m, m')$]. Spin-orbit coupling was not included, so the spin is conserved.

The symmetry of the octahedra (Fig. 1) is quite low as inversion is the only nontrivial symmetry operation allowed (C_i point group). Therefore, the five d -levels may have different energies and hybridization matrix elements among them are allowed. Notwithstanding that, we find that with the chosen axes off-diagonal dd -matrix elements on the Ag site are very small and were neglected.

Some linear combinations of p -orbitals are nonbonding and can be eliminated to reduce the Hilbert space. To this aim, we defined 5 symmetry adapted orbitals by the following transformation,

$$\tilde{P}_{\nu} = \frac{1}{\sqrt{\tilde{T}_{pd}(\nu)}} \sum_m t_{pd}(\nu, m) p_m$$

with

$$\tilde{T}_{pd}(\nu) = \sqrt{\sum_m |t_{pd}(\nu, m)|^2}.$$

This defines a set of orbitals with maximum overlap with the d -orbitals. Because of the low symmetry, the resulting orbitals are not orthogonal but are easily orthogonalized, resulting in new operators P_{ν} and hybridization matrix elements $T_{pd}(\nu)$ which expand the same maximally hybridized subspace. The orthogonalized orbitals (hereafter P -orbitals) have nearly the same symmetry as the original orbitals, so they can still be labeled as x^2-y^2 , xy ,

TABLE I: Crystal fields and hybridizations obtained from DFT and Wannier computations. The diagonal energies of P -orbitals in Eq. 2 are determined by $\varepsilon_P(\nu) = \Delta + e_P(\nu)$. All values are in eV. The last column are the expressions for the hybridizations in terms of the $x^2 - y^2$ matrix element and for a planar D_{4h} cluster used by Eskes *et al.*²⁴.

ν	AgF ₂ (C_i)			La ₂ CuO ₄ (D_{4h})		
	$\varepsilon_d(\nu)$	$e_P(\nu)$	$T_{pd}(\nu)$	$\varepsilon_d(\nu)$	$e_P(\nu)$	$T_{pd}(\nu)$
z^2	-0.25	0.32	1.51	0	$\frac{4}{5}T_{pp}$	$\frac{1}{\sqrt{3}}T_{pd}^\dagger$
$x^2 - y^2$	-0.28	-0.16	2.76	0	$-\frac{6}{5}T_{pp}$	T_{pd}^\dagger
xy	0.34	-0.05	1.36	0	$\frac{4}{5}T_{pp}$	$\frac{1}{2}T_{pd}^\dagger$
xz	0.09	-0.14	1.05	0	$-\frac{1}{5}T_{pp}$	$\frac{1}{2\sqrt{2}}T_{pd}^\dagger$
yz	0.10	0.04	1.02	0	$-\frac{1}{5}T_{pp}$	$\frac{1}{2\sqrt{2}}T_{pd}^\dagger$

[†] ($x^2 - y^2$) symmetry.

etc. Furthermore, they have small interorbital PP and Pd matrix elements between orbitals of different symmetry. We checked that keeping these matrix elements did not change the results significantly, therefore for simplicity they were also neglected.

The resulting Hamiltonian of the (AgF₆)⁴⁻ cluster reads

$$\begin{aligned}
 H = & \sum_{\nu} \varepsilon_d(\nu) d_{\nu}^{\dagger} d_{\nu} + \sum_{\nu} \varepsilon_P(\nu) P_{\nu}^{\dagger} P_{\nu} \\
 & + \sum_{\nu} T_{pd}(\nu) (d_{\nu}^{\dagger} P_{\nu} + P_{\nu}^{\dagger} d_{\nu}) \\
 & + \sum_{\substack{\nu_1, \nu_2 \\ \nu_3, \nu_4}} U^{(dd)}(\nu_1, \nu_2, \nu_3, \nu_4) d_{\nu_1}^{\dagger} d_{\nu_2}^{\dagger} d_{\nu_3} d_{\nu_4}.
 \end{aligned} \quad (2)$$

Table I shows the one-body parameters deduced from the Wannier90 computation. Setting $T_{pd}(x^2 - y^2) = 2.76\text{eV}$, the values of the $T_{pd}(\nu)$ matrix elements are in very good agreement with the expressions²⁴ for a cluster with D_{4h} symmetry using a Slater-Koster parametrization and assuming $T_{pd}(xy) = T_{pd}(x^2 - y^2)/2$ (last column of Table I). The symmetrized P orbitals manifest a more evident deviation of square planar symmetry and the D_{4h} expressions are not accurate.

We define the CT parameter $\Delta = E(d^{10}\underline{L}) - E(d^9)$ where \underline{L} denotes a hole in the ligand and the energies are average of the indicated multiplets setting $T_{pd}(\nu) = 0$. Interactions with the neighboring atoms are absorbed in the definition of Δ . In the case of intracluster excitations in the insulating phase, we need to consider one hole in the cluster, making the interaction term in Eq. (2) irrelevant. The full Hamiltonian will become relevant for intercluster excitations.

III. RESULTS

The real part of the optical conductivity, σ_1 , for selected temperatures is shown in Figure 2. The spectra

can be divided into several regimes and their equivalent excitations: far-IR phonons (seen as red sharp peaks), mid-IR absorption (above 0.1 eV), and near-IR to ultraviolet (UV) absorption. The former two low-energy excitations will be discussed in a separate publication. The high energy spectrum (Fig. 2) can be decomposed into 3 major excitations. The strongest one is the high energy absorption centered at about 3.4 eV with an onset at approximately 1.75 eV. This absorption can be associated with a strong interband transition, which sits at energies close to our experimental data range limit. Similar behavior of a high energy absorption was well studied, in particular in the parent compound La₂CuO₄^{25,26}. In the latter case, a strong peak can be seen in the real part of the optical conductivity at about 2.2 eV with a broad tail down to 1.25 eV²⁵⁻²⁷ as we demonstrate in Fig. 2.

The strong peak at 2.2 eV in La₂CuO₄ is associated with the charge transfer transition between the O p band and Cu d band and was measured in various parent compounds of the cuprates family^{27,29}. Taking into account the resemblance of the experimental data between AgF₂ and La₂CuO₄ with the following supporting results of the theoretical analysis, we associate the strong high energy absorption in our data to the charge transfer excitation between the F p band to the Ag d band.

In addition to the absorption tail of the CT excitation, we detect a broad absorption band. A similar but much weaker absorption in the optical conductivity was already reported in previous works regarding the cuprates^{25,27,28,30-32} as can be seen in Fig. 2. Uchida *et al.*²⁵ demonstrated the appearance of a mid-infrared (MIR) absorption depicted as a sub-gap peak centered at about 0.5 eV in the real part of the optical conductivity of Sr doped La₂CuO₄. Falck *et al.*²⁸ showed that oxygen doping in La₂CuO_{4+ δ} results in a similar MIR absorption which is dominant in sample with $\delta = 0.014$ and reduced T_N of 250 K. On the other hand, in an undoped sample with $\delta = 0$ and $T_N = 322\text{ K}$ the MIR absorption is negligible as can be seen in Ref. 28 and in Fig. 2. The MIR band, which appears as a peak in the real part of the optical conductivity of doped samples, partially draws spectral weight from a higher energy range, thus diminishes the charge transfer excitation upon further doping²⁵. The intensity of the MIR band is of the order of the charge transfer excitation in undoped La₂CuO₄ and even stronger for intermediate doping levels^{25,28}. Since we detect a MIR-NIR absorption band which is weak compared to that of the CT excitation, we conclude that the AgF₂ is practically in its undoped phase, as intended.

We note here that the broad absorption below the CT excitation can be roughly decomposed into 2 modes centered at around 1 eV and 1.7 eV. As the sample is warmed up to room temperature, the 1.7 eV excitation seems to remain almost intact with respect to energy, while the 1 eV excitation seems to soften toward 0.8 eV. The two separate modes can be easily distinguished in the spectra measured at 300 K as shown in Fig. 2. As will be seen below, the CT excitation at 3.4 eV and the optical

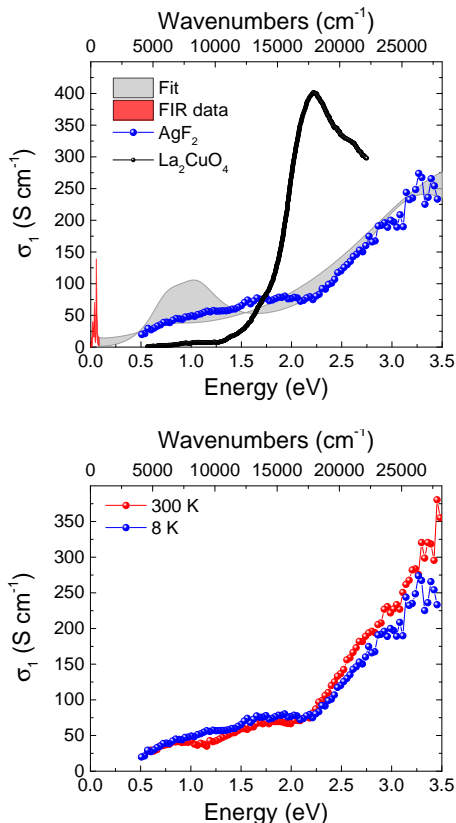


FIG. 2: Real part of optical conductivity for AgF_2 (this work). The top panel presents σ_1 as obtained from direct calculation of the pseudo-dielectric function using ellipsometry parameters Ψ_{ellip} and Δ_{ellip} for 2 angles of incidence as measured at a base temperature of 8 K. The shaded gray area represents the result of a fit to Ψ_{ellip} and Δ_{ellip} data separately (See appendix B) which reflects the confidence boundaries of our model with respect to the experimental data. Our data is compared with optical conductivity data adopted from Falck *et al.*^{26,28} on undoped La_2CuO_4 . The optical conductivity in the AgF_2 sample shows an onset at about 1.75 eV with high energy energy band transition which is associated with the charge transfer gap ($\Delta_{\text{peak}} \approx 3.4$ eV). The data on AgF_2 is compared with a charge transfer excitation peaking at $\Delta_{\text{peak}} \approx 2.2$ eV with an onset of ≈ 1.6 eV in the equivalent oxocuprates compound La_2CuO_4 . In addition the AgF_2 data shows a low spectral weight sub-gap absorption suggesting negligible doping as intended²⁸. Lower panel shows a comparison with data at 300 K showing slight modifications of the different excitations in the charge transfer sector and the sub-gap sector.

mode at 1.7 eV are consistent with a CT excitation and dd -excitations, respectively, as seen in the RIXS data. We also note a possible spectral weight transfer from the CT sector to the subgap excitations as a function of temperature and as shown in Fig. 2. However, the confidence boundary that we have on our optical conductivity

data in this range requires a further and more precise experimental investigation of this range to understand this spectral weight interplay as a function of temperature.

We now turn to the inspection of the XAS and RIXS data. F K -XAS on AgF_2 is compared to O K -XAS on La_2CuO_4 ³³ in Fig. 3 (top panel). The peak at the absorption threshold of La_2CuO_4 reflects the O $2p$ -Cu $3d$ hybridization and originates upon excitation to the Upper Hubbard Band (UHB) of predominantly $3d_{x^2-y^2}$ character in this material³³. Such p - d hybridized peaks have also been observed in F K -XAS of several $3d$ metal fluorides³⁴⁻³⁶. The broad structures ranging from ~ 531 eV to 537 eV reflect hybridizations between unoccupied O $2p$ and La $5d$ and $4f$ DOS. The sharp peak marked by the arrow in F K -XAS on AgF_2 , therefore represents excitations into Ag $4d$ orbitals via hybridization with F $2p$, reflecting the narrow UHB in AgF_2 ¹⁴. A good account of the XAS spectra can be obtained by comparing with the F-unoccupied density of states (DOS) of AgF_2 shown in Fig. 3 (bottom panel). The broad structures above the unoccupied d -band can be assigned to Ag $5s$ and $5p$ states which hybridize with F $2p$ states. The edge can be attributed to the hybridization of F $2p$ with Ag- $4d$. The weight of the $4d$ states in this region is approximately given by the difference between the total and the F $2p$ DOS.

Upon excitation at the F K edge, a well-resolved RIXS spectrum can be observed (Fig. 4). For comparison, O K -RIXS spectrum of La_2CuO_4 is also presented in Fig. 4 (Left panel) with overall remarkably similarity, which facilitates the assignment of the features and further supports the claim that silver fluorides are excellent cuprate analogues.

In the insets of the middle panel in Fig. 4, we show that the low-energy part of the AgF_2 spectrum can be decomposed into an elastic peak (0 eV), phonons (0.041 eV) and their overtones and a damped bimagnon peak (centered at 0.218 eV). The energy of the assigned bimagnon peak corresponds to that observed in the Raman spectra ($\sim 3J$)¹⁴. Bimagnons can be probed also with K -edge RIXS, as observed in the O K -RIXS on La_2CuO_4 in the MIR region³⁷. However, to accurately determine spectral contributions of the phonon progression and the bimagnon peak in AgF_2 , momentum-resolved RIXS is desirable.

As shown in Fig. 4 (middle panel) a series of excitations at 1.59, 1.86, and 2.33 eV resemble the well-known dd -excitations of cuprates³⁷, an assignment which will be substantiated below. At high energies (> 4 eV), the RIXS spectrum is dominated by a broad feature with a strong resonance behavior as a function of the incident energy. We attribute the resonance to the excitation of CT-transitions involving an Ag site and its neighbouring F's as will be also explained below. Between the pd and the dd -excitations, a peak is observed at 3.32 eV. The energy scale of this peak matches reasonably well with the growing optical conductivity of AgF_2 shown in Fig. 2. As such, this peak can be assigned to transitions across

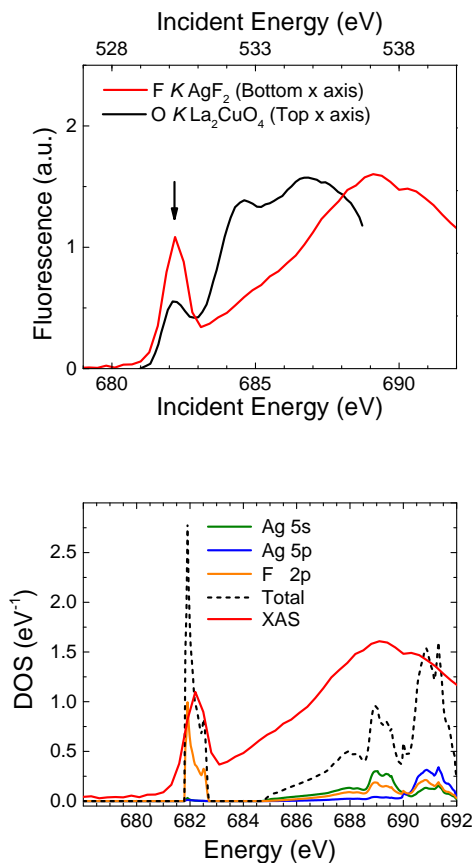


FIG. 3: Top panel: Comparison of F K -XAS on AgF_2 and O K -XAS on La_2CuO_4 ³³. AgF_2 and La_2CuO_4 XAS energies correspond to the bottom and the top x -axes, respectively. Bottom panel: Orbital projected unoccupied DOS of AgF_2 from the unpolarized DFT computations. The Fermi level has been shifted to 681.8 eV to facilitate comparison with F K -XAS (red line). The total unoccupied DOS, includes contributions from the shown symmetries above the edge as well as Ag $4d$ which will be shown later (Fig. 5(a)). For the band at the Fermi level, it is nearly equal to the difference of the total and F 2p contribution.

the CT gap from an Ag site to more distant F's and provides further confirmation of the larger fundamental gap in AgF_2 than La_2CuO_4 . Both the dd - and CT-excitations are discussed in detail below.

The map in Fig. 4 (right panel) shows energy-detuned RIXS spectra collected across the F K -XAS. Energy-detuned RIXS is very useful for revealing the degree of localization of the excitations. At higher incident photon energies (> 683 eV), two fluorescence emission lines arise. We can view the fluorescence RIXS as an incoherent process, that is, the excitation and de-excitation are decoupled from each other. Electrons are excited from F $1s$ core level to unoccupied valence states involving Ag $5s$, Ag $5p$, and F $2p$ (shown in Fig. 3, bottom panel).

The de-excitation is from the broad valence states to refill the $1s$ core hole resulting in a characteristic emission energy. In other words, the energy loss of fluorescence varies linearly with the incident energy. Across the resonance of the UHB peak (682.2 eV), dd -excitations and the CT-excitations resonate at the UHB peak and show an almost fixed energy loss, i.e., Raman-like, indicating the energy loss corresponds to the energy of fixed-number-of-particle excitations (i.e. excitons, particle-hole, etc.). The localized dd - and CT-excitations are very common in many transition metal oxides (including oxocuprates).

Figure 5 (top panel) shows the local DOS projected on the different d -orbital symmetry in the nonmagnetic (metallic) solution with the abscissa origin set at the Fermi energy. Due to the stronger hybridization compared to other symmetries (c.f Table I), the antibonding $d_{x^2-y^2}$ band is half-filled and is well separated from the other (filled) d -bands. Panel (b) shows the joint DOS between the unoccupied $d_{x^2-y^2}$ and occupied orbitals of the other symmetries representing dd -transitions with a constant matrix element. Averaging over the four possible final states (black line), one obtains a line shape surprisingly similar in position and overall shape to the dd -RIXS spectra despite neglecting matrix element effects. The theoretical line shape is broader than the experiment, which can be attributed to correlation-induced band narrowing effects absent in DFT. Neglecting minor differences, this analysis allows to assign the lower shoulder to transitions of the $d_{x^2-y^2}$ hole to z^2 orbitals, the higher peak to transitions to mainly xz orbitals and the intermediate band to a mixed character. Such assignments are in general good agreement with previous works regarding fluoroargentates³⁸⁻⁴². Notice, however, that here the peaks tend to have a mixed symmetry which can be attributed to the influence of the ligand orbitals which depart strongly from D_{4h} -symmetry as discussed in Sec. IID.

The good agreement of the metallic DFT solution with the dd -transitions of the correlated insulator may seem at first sight surprising. However, such a result would be completely spoiled if a magnetic DFT solution is used as all orbitals with $\nu_2 \neq \nu_1$, except the majority one (say $\nu_1 = d_{x^2-y^2\uparrow}$), would be shifted by $U^{(dd)}(\nu_1, \nu_2, \nu_2, \nu_1)n_{\nu_1}$ with n_{ν_1} the average hole occupancy. Instead, such a large shift is not operative in a real dd -transition as it is essentially a one-particle process and the onsite Coulomb interaction is not involved. The nonmagnetic computation, instead, avoids the large Coulomb shift and includes only shifts due to the ligand and crystal fields which are the relevant ones.

An alternative description of the excitations, which emphasizes the local character, can be obtained with the cluster model presented in Sec. IID. Figure 6 shows the energy levels of the one-hole configuration of the cluster for AgF_2 and a cuprate²⁴. The dashed lines on the left (right) of each panel are the d^9 ($d^{10}\underline{L}$) configurations. Each left-right pair of a given symmetry produces a bonding and antibonding level upon hybridization shown with

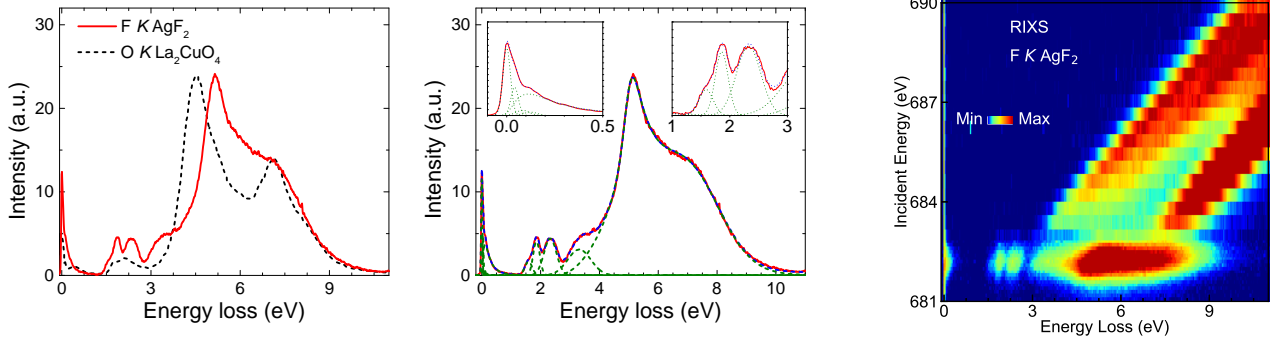


FIG. 4: Left panel: Comparison of F K -RIXS on AgF_2 and O K -RIXS on La_2CuO_4 ³⁷. Middle panel: F K -RIXS on AgF_2 fitted with multiple components (see text). Insets show the low-energy inelastic features and dd -excitations with fitted profiles. Right panel: F K -RIXS incident energy map on AgF_2 showing Raman and fluorescence features.

the full lines. Notice that because we are showing hole energies, the bonding (antibonding) states are at high (low) energies. Energies are measured with respect to the $x^2 - y^2$ ground state, so the vertical scale represents the energy of transitions to the different excited states. In addition, following Ref. 43 the energy of the ground state has been lowered by J , the magnetic stabilization energy due to the interaction with the neighbors. We have added one time J and not $2J$ since we have broken bonds with the neighbors while Ref. 43 considered a cluster with 5 Cu's and excited ferromagnetic alignment of spins.

The first striking difference between cuprates and AgF_2 is that the $d^{10}\underline{L}$ configurations have much smaller splittings in the fluoride (cf. panels a and b in Fig. 6). This is in part a consequence of smaller F-F hoppings¹⁴. Optimized p Wannier orbitals have large crystal fields splittings parametrized by $\varepsilon_p(m)$ in Eq. 1, but they get averaged out when projected on the d -symmetrized states. Notice that in the case of cuprates, T_{pp} lowers the energy of the $x^2 - y^2$ ligand orbital while the hybridization with the $d_{x^2-y^2}$ rises it resulting in a bonding $x^2 - y^2$ orbital at 4.8 eV slightly above the yz and xz orbitals. In the case of AgF_2 , the lowering effect of T_{pp} is almost absent so the $x^2 - y^2$ bonding orbital is at much higher energies. This crossing of levels can be visualized in the Tanabe-Sugano diagram of Fig. 6(c) (upper yellow line).

As a reference, we first discuss the case of cuprates for which we used one of the parameter sets considered by Eskes *et al.* for CuO in Ref. 24 and reproduced in Table II (labeled as Local in the La_2CuO_4 sector). The parameter Δ corresponds to the value quoted by Eskes *et al.* using a slightly different definition, namely, $\Delta - T_{pp}/5 = 2.2\text{eV}$. From Fig. 6(b) we see that this set of parameters gives a quite good estimate of dd -transition energies. As a bonus, this analysis suggests that the main structure seen in RIXS near 5 eV is a charge transfer transition from the ground state of mainly $d_{x^2-y^2}$ character to a hole in a combination of ligand orbitals with yz or xz symmetry. This is the lowest energy pd -transition within the cluster

so its referred to as a "local" CT-transition.

The position and ordering of dd -transitions predicted in Ref. 24 and partially reproduced in Fig. 6(b) was studied with the advent of RIXS two decades latter. A detailed analysis⁴⁴ of the angular dependence of RIXS matrix elements confirmed the ordering and provided a refinement of the energies. Using a more ionic parameters set with a larger fundamental gap (last column in Table II) do not produce a satisfactory agreement. We will come later to this important point. Notice that the parameters in panel (a) have been adjusted ad hoc to fit the experiment while no such adjustment has been done for panel (b), which yields a slightly less accurate agreement for dd -excitations.

For AgF_2 , we found that DFT parameters of Table I give a first Ansatz for the position of RIXS structures including the DFT value for the CT parameter, $\Delta_{DFT} = 1.29\text{ eV}$, however it underestimates the energy of the dd -transitions. This can be corrected by increasing the T_{pd} matrix elements by 20% as shown in the Tanabe-Sugano diagram of Fig. 6(c) and panel(a). In this way, the energies of the dd -transitions match the experimental ones but, due to the low symmetry of the cluster, the lines should be understood as averages of the structures shown in Fig. 5(b) and a one-to-one correspondence of peaks and dd -lines is oversimplified. On the other hand, this analysis suggests that also for the fluoride, the main peak in RIXS near 5 eV can be assigned to the local CT transition with a final state consisting in a hole in an orbital with xz or yz symmetry and mainly F character [c.f. Fig. 6(a)].

The increase of T_{pd} should not be taken too seriously as it may just reflect longer range hopping process from the $d_{x^2-y^2}$ and non-magnetic stabilization terms of the $x^2 - y^2$ ground state due to intercluster interactions beyond the magnetic correction introduced above. More importantly, increasing Δ with respect to the DFT value (i.e. increasing the ionicity) monotonously decreases the energy of dd -transitions (i.e., worsening the agreement). We conclude that the description of dd -transitions re-

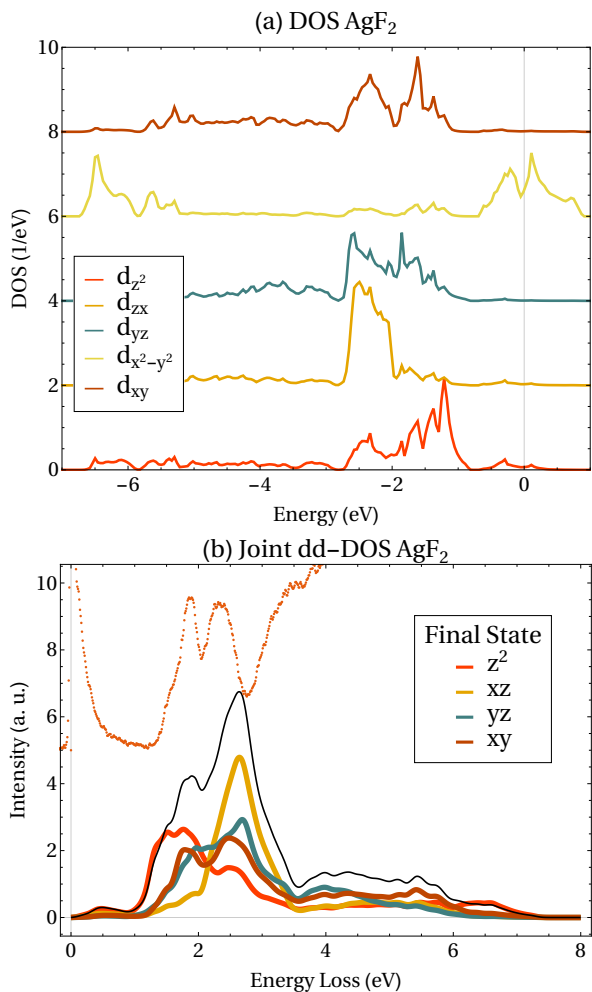


FIG. 5: (a) DOS of AgF_2 projected on Ag d orbitals from the unpolarized DFT computations. (curves have been shifted by $2/\text{eV}$ for clarity). The Fermi level is at zero energy. (b) joint DOS between the unoccupied DOS of $d_{x^2-y^2}$ character and occupied DOS of different character representing dd -transitions of a hole from the half-filled $d_{x^2-y^2}$ to a final state (labeled by the final state) character. The thin black line is the average of the different contributions. The dotted line is the experimental RIXS data.

quires a quite covalent ground state in AgF_2 . This is confirmed by the previous analysis of the joint DOS in Fig. 5, which is based on the same DFT computation.

We now compare our theoretical analysis with the optical transitions. For a clean insulator, optical excitations measure the direct gap of the material. More precisely, the optical absorption may or may not show sharp transitions corresponding to particle-hole bound states (excitons), but should show an edge to a continuum of states. The threshold of the continuum corresponds to the minimum energy to separate an electron and a hole at an infinite distance and zero total momentum and defines the fundamental gap. We refer to these CT transitions as

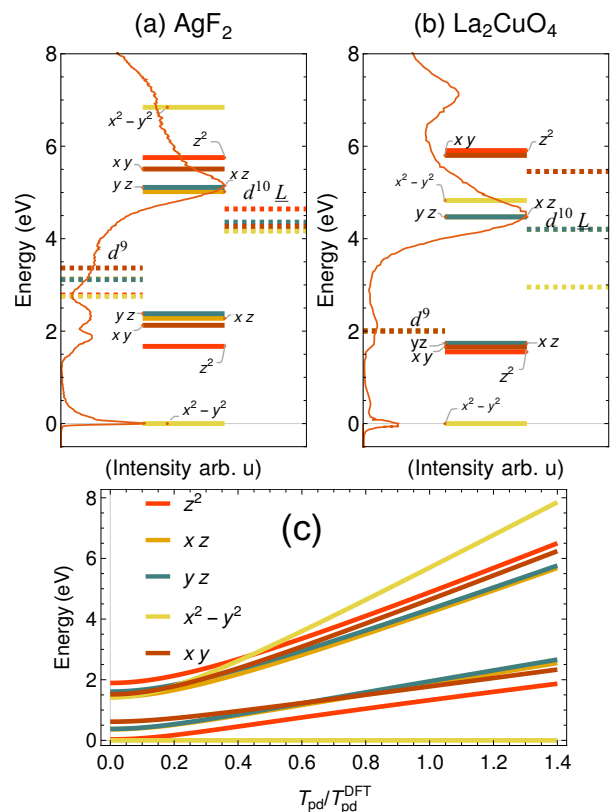


FIG. 6: Energy level diagram for one hole states in the clusters considered for (a) AgF_2 with $\Delta = 1.29$ eV and parameters from Table I with a 20% increase of the T_{pd} matrix elements and $J = 70\text{meV}$ as stabilization energy.⁴³ (b) La_2CuO_4 with $\Delta = 2.45$ eV and $J = 130\text{meV}$. Dashed lines correspond to energies before hybridization in the d^9 configuration (left) and $d^{10}\underline{L}$ (right). Hybridization yields bonding and antibonding states (full lines). The ground state corresponds to the half-filled antibonding $d_{x^2-y^2}$ which was placed at zero energy so the vertical scale represent energies of transitions to states of majority d^9 character (i.e. dd -transitions) around 2eV and $d^{10}\underline{L}$ (i.e. charge transfer transitions) at higher energy. RIXS spectra has been superposed for comparison. (c) shows the Tanabe-Sugano diagram for dd - (lower lines set) and charge transfer transitions (higher lines set). Position of excited states are measured with respect to the $x^2 - y^2$ ground state and are plotted as a function of the renormalization of the T_{pd} matrix element with respect to the DFT value. The magnetic stabilization energy of the $d_{x^2-y^2}$ state mentioned in the text has been omitted.

"non-local". From the optical experiments, we obtained lower and higher bounds for the fundamental gap using two different methods: i) a linear extrapolation of the edge giving a lower bound and ii) a fit with a sharp edge broadened with a Gaussian distribution giving a higher bound. We estimate $E_{gap} = 1.8 \pm 0.1$ eV for La_2CuO_4 and $E_{gap} = 2.2 \pm 0.3$ eV for AgF_2 .

TABLE II: Comparison of parameter sets appropriate for local and non-local excitations and resulting fundamental gap for AgF_2 and La_2CuO_4 . We also show the numbers of holes in the transition metal n_d .

	$\text{AgF}_2 (C_i)$		$\text{La}_2\text{CuO}_4 (D_{4h})$	
	Local	Non-local	Local	Non-local
Δ	1.29	2.8	2.45	2.95
T_{pd}^\dagger	3.31	2.76	2.3	2.5
T_{pp}	0.15*	0.15*	1.25	1.0
F^0	6.48	6.48	6.81	7.31
F^2	8.19	8.19	11.41	11.41
F^4	6.80	6.80	7.31	7.31
E_{gap}	1.54	2.25	1.27	1.8
n_d	0.60	0.73 [†]	0.60	0.66

[†] ($x^2 - y^2$) symmetry.

*For AgF_2 we used crystal field parameters from Table I.

For comparison we defined an effective

$$T_{pp} = [e_P(xz) + e_P(yz)]/2 - e_P(x^2 - y^2).$$

[†] Since the charge balance is determined by local transitions the physical value should be considered as the one computed with Δ in the Local column.

Neglecting the band formation effects, we can estimate the fundamental gap as the minimum energy to extract an electron from one cluster and add it to another cluster, i.e. $E_{gap} \equiv E_0(N+1) + E_0(N-1) - 2E_0(N)$. This energy corresponds also to the effective U_{eff} in a one-band model which for cuprates provides a good description of the main charge transfer absorption band in optics⁴⁵. $E_0(N-1)$ corresponds to the ground state of the two-hole multiplet ($d^8 + d^9 \underline{L}$) which is the Zhang-Rice state. The $N+1$ configuration corresponds to the filled shell so there is no multiplet but a unique state (d^{10}).

To compute the fundamental gap, we solved the many-body problem in the cluster using Lanczos exact diagonalization as implemented in the Quany package⁴⁶. The Coulomb interaction in Eq. (2) was parametrized in terms of Slater integrals. For Cu we used the values corresponding to the Racah parameters of Ref. 24. For Ag we took the values corresponding to the Racah parameters of Ref. 9 for F^2 and F^4 and took F^0 to be larger in view of the reduced screening expected in a fluoride with respect to an oxide¹⁴. Table II shows the resulting fundamental gap for the various parameters chosen. Both for AgF_2 and La_2CuO_4 the parameters that fit well the dd -transitions (labeled Local) correspond to E_{gap} smaller than the one measured with optics. The effect is much stronger in AgF_2 which requires a quite small CT parameter to fit the dd -transitions and yet has a larger experimental E_{gap} than cuprates. Notice that a small Δ does not imply that the local CT transitions are at small energy. Indeed, the local Δ represents the difference in energy between the levels before hybridization (difference between left and right multiplets with dashed lines in the top panels of Fig. 6). Instead, the local CT transition energies are set by the difference between hybridized levels (full lines in

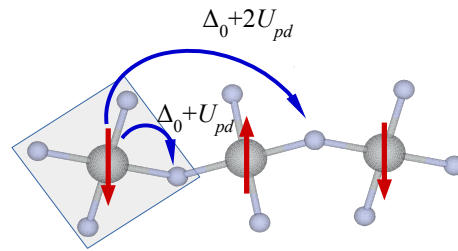


FIG. 7: Charge transfer processes within the AgF_6 cluster (gray region) and to a distant fluorine.

Fig. 6).

We argue that the difference in Δ needed to fit optics (labeled Non-local) and RIXS (Local) reflects interactions beyond the on-site ones considered in Eq. (2). In particular, adding a nearest neighbor repulsion between p and d orbitals, U_{pd} , renormalizes Δ in a different way for local (intra-cluster) and nonlocal (inter-cluster) CT excitations as shown schematically in Fig. 7. In the ionic limit, the effective Δ for local excitations ($d^9 \rightarrow d^{10} \underline{L}$) is $\Delta^{\text{loc}} = \Delta_0 + U_{pd}$ while it enters as $\Delta^{\text{nl}} = \Delta_0 + 2U_{pd}$ in the nonlocal excitations that define the fundamental gap. Here we define the difference of one-hole diagonal energies in the absence of Coulomb interactions, $\Delta_0 = \bar{\epsilon}_p^0 - \bar{\epsilon}_d^0$ and bar indicates average over the multiplet. Taking the difference of the first and second column Δ for each material, this implies a $U_{pd} \approx 0.5 \pm 0.2$ eV for cuprates (consistent with the accepted value) and $U_{pd} \approx 1.5 \pm 0.5$ eV for AgF_2 , a value much larger than in cuprates.

IV. DISCUSSION

AgF_2 is emerging as a highly interesting cuprate analogue which merits a detailed analysis of similarities and differences with its siblings. We have shown, on the one hand, that the neutral dd -transitions are remarkably similar in the two materials. On the other hand, the fundamental gap and high energy CT excitation energies are about 20% larger in AgF_2 . This dichotomy between very good matching in one type of experimental probe and a substantial difference in another type of probe is a robust feature which can be appreciated by a direct examination of the spectra. The theoretical analysis allows to explore the implications of these observations and connect with other works.

In general, U_{pd} matrix elements will be orbital dependent, so our estimate above should be considered as a multiplet average. Coming back to the original p operators, the Hamiltonian for the nearest neighbor Coulomb repulsion in one Ag-F bond can be written as

$$H_{\text{bond}} = \sum_{\nu, m} U_{pd}(\nu, m) d_\nu^\dagger d_\nu p_m^\dagger p_m.$$

We expect that also off-diagonal terms will be present,

in particular

$$H'_{bond} = \sum_{\nu \neq \mu, m} W_{pd}(\nu, \mu, m) d_{\nu}^{\dagger} d_{\mu} p_m^{\dagger} p_m + h.c.$$

in which a hole in a p -orbital induces a dd -transition. This last operator naturally explains the RIXS activity for dd -transitions at the ligand K-edge and can be used to evaluate the cross section. We expect that U_{pd} and W_{pd} have a similar material dependence so the larger RIXS activity for dd -transitions in AgF_2 with respect to the cuprates (cf. panels (a) and (b) in Fig. 6) is an indirect confirmation of the large intersite interactions.

The band structure of hybrid DFT computations¹⁴ shows a smaller gap for AgF_2 than for La_2CuO_4 despite the fundamental gap in optics appears to have the opposite behavior. This should not be taken as a deficiency of DFT which is a theory which is aimed at the density, not the spectral function, so a small gap in the DFT Kohn-Sham spectrum just indicates a more covalent material. Indeed, model computations⁴⁷ show that the Kohn-Sham gap in exact DFT is determined by the energy cost of neutral (i.e., local) excitations ($\Delta_0 + U_{pd}$ in our case) and not the non-local ones determining the fundamental gap $\Delta_0 + 2U_{pd}$. This gives further support to our finding that the DFT value for Δ has the right magnitude for describing neutral (local) transitions and indicates strong covalency⁴⁸ in the ground state despite a large fundamental gap.

The large value of $U_{pd} \approx 1.5 \pm 0.5$ eV for AgF_2 poses a stability problem as it implies $\Delta_0 \approx -0.2 \pm 0.8$ which would make AgF_2 a negative charge transfer system as AgO . Taken literally and in the ionic limit, holes should populate the ligands as it occurs in formally d^9 , silver oxide⁹. This can be avoided if one assumes that also intra and inter site F-F Coulomb repulsions are present which can stabilize the d^9 state. At present, the indeterminacies are too large and it could be that Δ_0 is small but positive. In any case, our results point to AgF_2 being close to a charge transfer instability. In this regard, it is very suggestive that besides the magnetic brown α - AgF_2 considered in this study, a metastable red-brown diamagnetic β phase has been reported⁴⁹, which has been interpreted in terms of a disproportionated (Charge Density Wave) ground state. Although the structure of the β phase is not known, DFT computations^{50,51} find a CDW polymorph very close in energy with respect to the usual antiferromagnetic phase, which also points to AgF_2 being at the verge of a charge-transfer instability.

V. CONCLUSIONS

We have measured the optical conductivity and resonant inelastic X-ray scattering spectra of AgF_2 to study its electronic excitations. We observe a charge transfer excitation between the F p bands and the Ag d bands peaking at about 3.4 eV in both optical conductivity and RIXS spectra. We resolve several dd -excitations at 1.59,

1.86 and 2.33 eV from the RIXS spectra. We performed DFT and cluster calculations of the electronic structure which allowed to identify dd -excitations and local CT-transitions at high energy and a "non-local" CT transition determining the optical gap.

Using DFT and cluster computations, we provided estimates of the fundamental electronic parameters of this emerging quantum material, which are essential for future theoretical studies. The similarity between our data and that of the charge transfer insulator La_2CuO_4 is striking, but the subtle differences encode very interesting new physics. In particular, AgF_2 is predicted to be close to a charge-transfer instability due to a quite large value of U_{pd} . Interestingly, this parameter has been considered essential in some theories of cuprates⁵² so a material with an enhanced U_{pd} can provide key clues to its role in determining the physics of cuprates.

Since the superconductivity in cuprates appears close to an insulating magnetic phase, while the same phenomenon in doped BaBiO_3 appears in close proximity of the insulating CDW phase, we expect a bright future in the search for doped⁵³ and hopefully superconducting⁵⁴ phases of AgF_2 which seems to combine both instabilities in the same material.

ACKNOWLEDGMENTS

We acknowledge J. Teyssier for his help with the ellipsometry measurements. This work was supported by the Swiss National Science Foundation through projects 200020-179157 and CRFS-2-199368. W.G. acknowledges Polish National Science Centre (Maestro grant 2017/26/A/ST5/00570). Z.M. acknowledges the financial support of the Slovenian Research Agency (research core funding No. P1-0045; Inorganic Chemistry and Technology). We acknowledge Diamond Light Source for providing the beamtime under the proposal NR24869 on the Beamline I21. P.B., G.G. and J.L. acknowledge support from MIUR Italian Ministry for Research through PRIN Project No. 2017Z8TS5B. J. L. acknowledges financial support from Regione Lazio (L. R. 13/08) under project SIMAP.

AUTHOR CONTRIBUTIONS

K.K. and J.G. contributed equally to this work. The sample was synthesized by Z.M. and shock-compressed by W.T. and J.P. N.B., K.K. and J.G. carried out the optical spectroscopy measurements. Data analysis of the optical conductivity was done by N.B. and D.v.d.M. A.N. and K.Z. carried out the RIXS experiment. Data analysis of the RIXS data was carried out by A.N., K.Z. and G.G. R.P. P.B. and J.L. performed DFT and cluster calculations of the electronic structure. W.G. and J.L. conceived and supervised the entire project. N.B. and J.L. wrote

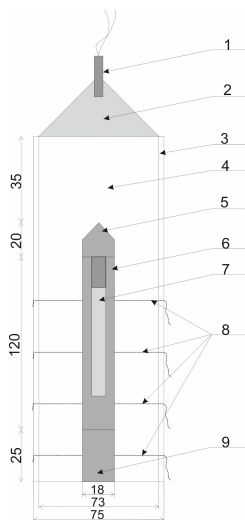


FIG. 8: Experimental setup for explosive compaction. 1 – electric detonator, 2 – plane wave generator, 3 – PVC tube, 4 – explosive, 5 – upper plug together with conical hat, 6 – container with compacted sample, 7 – compacted sample, 8 – short circuit sensors for measuring the detonation velocity, 9 – momentum trap. Dimensions are given in mm on the left-hand side.

the manuscript with inputs and comments from all coauthors.

Appendix A: Sample preparation procedure

A few gram sample of AgF_2 has been placed inside of a 99.99% Cu container (Figure 8), pressed manually using a copper cylinder, and the upper plug has been hammered into the container for even better compactness. All operations were carried out inside an argon-filled glovebox.

Explosive compaction has been performed using three distinct types of explosives; their composition and results of measurements of the detonation velocity are presented in Table III. Consecutive explosions were carried out using the same container, but changing only parts 5 and 9 each time (*cf.* Figure 8), due to their severe shock deformation.

Samples were undergoing explosive compaction in the following way:

I one sample underwent only type A explosion,

II one sample underwent consecutive type A and B explosions,

III one sample underwent consecutive type A, B and C explosions.

Data on high-pressure behavior of silver fluorides up to 40 GPa¹⁶ were used to calculate the compression shock curve of the crystalline AgF_2 . The equation of state of

a multicomponent medium (solid-gas)⁵⁵ was used to describe the physical properties of the porous AgF_2 samples loaded by a shock wave. To estimate the temperature in the shock compressed sample, the dependence of specific heat on temperature for AgF_2 ¹⁴ was extrapolated to high temperatures. It was assumed that the entire energy of the shock compression of a porous sample is converted into heat, which causes the sample temperature to rise. The initial density of the samples was 3.14 g/cm^3 . It was estimated that during the type A explosion, the maximum pressure in the sample was ca. 11 GPa, the maximum temperature was ca. 1500 °C and the density after loading was 5.1 g/cm^3 . The explosion B in procedure II resulted in substantially increased maximum pressure (63 GPa), but the temperature reached only 2100 K. The density of the samples after the loading B was 5.4 g/cm^3 . In the type C explosion (procedure III), the estimated pressure was 73 GPa and the temperature was 2000 K. Since the copper container did not explode, it was presumed that the pressure increase has substantially hindered the thermal decomposition of AgF_2 with the release of F_2 gas. Copper container was cut into pieces in an inert gas atmosphere. Indeed, visual inspection of the sample indicated that thermal decomposition and partial erosion of the container occurred only in the part of the sample adjacent to the container inner wall, while the inside of the sample cylinder was dark brown as typical for AgF_2 . X-ray diffraction analysis revealed that the samples undergoing the procedure III were nearly pure AgF_2 , and the apparent density of the sample was ca. 95% of the crystallographic density; a small fraction of the sample might be amorphous.

Appendix B: Ellipsometry data

We measured the complex dielectric function using a Woollam VASE[®] spectroscopic ellipsometer in the energy range from 0.55 eV to 3.5 eV. The reflectivity ratio for p and s polarization is defined as

$$r_p/r_s = \rho = \tan(\Psi_{\text{ellip}})e^{i\Delta_{\text{ellip}}}$$

where Ψ_{ellip} and Δ_{ellip} are the parametric amplitude and phase difference components of the complex reflectivity

Type	Explosive	Density [g/cm ³]	D [m/s]
A	Ammonal 2% (98% ammonium nitrate + 2% aluminum powder)	0.77	2600
B	Emulsion explosive (EmEx, mostly ammonium nitrate + fuel oil + water)	1.17	5300
C	Emulsion explosive (EmEx) + 20% 1,3,5-trinitro-1,3,5-triazinane (RDX)	1.25	5700

TABLE III: Explosives used for consecutive explosive compaction and their detonation velocities, D .

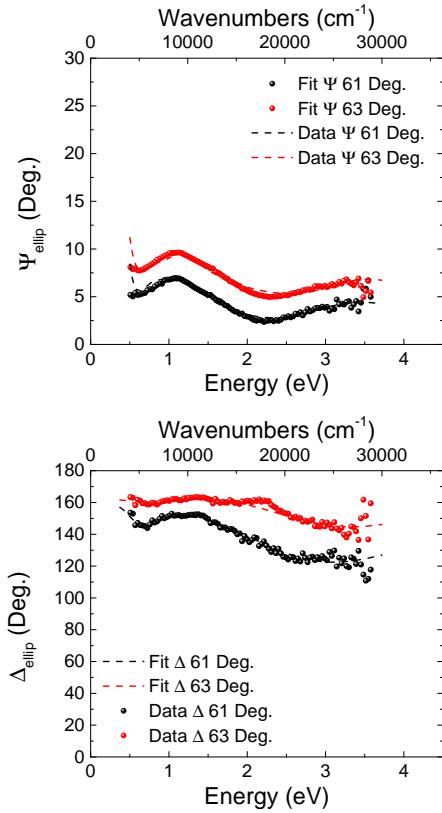


FIG. 9: The ellipsometric parameters Ψ_{ellip} and Δ_{ellip} as measured at temperature of 8 K for AOI of 61 (black spheres) and 63 (red spheres) degrees. The corresponding model fit as explained in the appendix is shown in dashed lines.

ρ . We measured the r_p/r_s ratios at incident angles θ of

61° and 63° at selected temperatures of 300 K, 250 K, 226 K, 200 K, 176 K, 150 K, 100 K, 50 K and 8 K. The corresponding $\Psi(\omega)$ and $\Delta(\omega)$ spectra for 2 angles of incidence measured at the lowest temperature are displayed in Figure 9.

We fitted $\Psi(\omega)$ at two different angles of incidence (AOI) simultaneously following a similar but a separate fit to the $\Delta(\omega)$ spectra at two different angles of incidence using a Drude-Lorentz parametrization of $\epsilon(\omega)$. For the powder pressed sample of AgF_2 , we have used an isotropic model for $\epsilon(\omega)$. The confidence boundaries presented in Fig. 2 of the main text represent the possible range of σ_1 values between the two limits, i.e. a fit to Ψ_{ellip} data (2 AOI) and a fit to Δ_{ellip} data (2 AOI), thus reflecting our error bar for the reported results. A simultaneous fit to both Ψ_{ellip} and Δ_{ellip} was not possible to obtain under the use of a simple one layer model of $\epsilon(\omega)$ for the AgF_2 sample. We assume that the discrepancy is due to the polycrystalline nature of the sample. Nevertheless, the impact of this discrepancy is mostly shown around the 1 eV absorption while the CT excitation is robust for both analysis procedures.

To extract the optical conductivity directly from the r_p/r_s ratio, we have used the following pseudo-dielectric function:

$$\epsilon_{ps} = \sin^2(\theta) \left[1 + \tan^2(\theta) \left(\frac{1 - \rho}{1 + \rho} \right)^2 \right]$$

where $\sigma = -i\nu 2\pi c \epsilon_0 (\epsilon_{ps} - 1)$ is the optical conductivity in units of S/cm as shown in Fig. 2 for the real part. Here ν are wavenumbers in cm^{-1} , c is the speed of light in vacuum in m/s and ϵ_0 is the vacuum permittivity in F/m.

* nimrod.bachar@unige.ch

† jose.lorenzana@uniroma1.it

¹ M. Cyrot, B. Lambert-Andron, J. Soubeyroux, M. Rey, P. Dehauht, F. Cyrot-Lackmann, G. Fourcaudot, J. Beille, and J. Tholence, *Journal of Solid State Chemistry* **85**, 321 (1990).

² R. Viennois, E. Giannini, J. Teyssier, J. Elia, J. Deisenhofer, and D. V. der Marel, *Journal of Physics: Conference Series* **200**, 012219 (2010).

³ F. Deslandes, A. Nazzal, and J. Torrance, *Physica C: Superconductivity* **179**, 85 (1991).

⁴ F. Wang and T. Senthil, *Physical Review Letters* **106** (2011).

⁵ K. Wang, N. Bachar, J. Teyssier, W. Luo, C. W. Rischau, G. Scheerer, A. de la Torre, R. S. Perry, F. Baumberger, and D. van der Marel, *Physical Review B* **98** (2018).

⁶ X. Chen, T. Hogan, D. Walkup, W. Zhou, M. Pokharel, M. Yao, W. Tian, T. Z. Ward, Y. Zhao, D. Parshall, C. Opeil, J. W. Lynn, V. Madhavan, and S. D. Wilson, *Physical Review B* **92** (2015).

⁷ A. de la Torre, S. M. Walker, F. Bruno, S. Ricco,

Z. Wang, I. G. Lezama, G. Scheerer, G. Giriat, D. Jaccard, C. Berthod, T. Kim, M. Hoesch, E. Hunter, R. Perry, A. Tamai, and F. Baumberger, *Physical Review Letters* **115** (2015).

⁸ D. Li, K. Lee, B. Y. Wang, M. Osada, S. Crossley, H. R. Lee, Y. Cui, Y. Hikita, and H. Y. Hwang, *Nature* **572**, 624 (2019).

⁹ L. H. Tjeng, M. B. J. Meinders, J. van Elp, J. Ghijsen, G. A. Sawatzky, and R. L. Johnson, *Phys. Rev. B* **41**, 3190 (1990).

¹⁰ S. E. McLain, M. R. Dolgos, D. A. Tennant, J. F. Turner, T. Barnes, T. Proffen, B. C. Sales, and R. I. Bewley, *Nat. Mater.* **5**, 561 (2006).

¹¹ Z. Mazej, E. Goreschnik, Z. Jaglić, B. Gawel, W. Łasocha, D. Grzybowska, T. Jaroń, D. Kurzydłowski, P. Malinowski, W. Koźminski, J. Szydłowska, P. Leszczyński, and W. Grochala, *CrystEngComm* **11**, 1702 (2009).

¹² W. Grochala, *Nat. Mater.* **5**, 513 (2006).

¹³ D. Kurzydłowski, Z. Mazej, Z. Jaglić, Y. Filinchuk, and W. Grochala, *Chem. Commun.* **49**, 6262 (2013).

¹⁴ J. Gawraczyński, D. Kurzydłowski, R. A. Ewings, S. Ban-

- daru, W. Gadomski, Z. Mazej, G. Ruani, I. Bergenti, T. Jaroń, A. Ozarowski, S. Hill, P. J. Leszczyński, K. Tokár, M. Derzsi, P. Barone, K. Wohlfeld, J. Lorenzana, and W. Grochala, *Proceedings of the National Academy of Sciences* **116**, 1495 (2019).
- ¹⁵ T. Jaroń and W. Grochala, *Phys. status solidi – Rapid Res. Lett.* **2**, 71 (2008).
- ¹⁶ A. Grzelak, J. Gawraczyński, T. Jaroń, D. Kurzydłowski, A. Budzianowski, Z. Mazej, P. J. Leszczyński, V. B. Prakapenka, M. Derzsi, V. V. Struzhkin, and W. Grochala, *Inorg. Chem.* **56**, 14651 (2017).
- ¹⁷ D. Kurzydłowski and W. Grochala, *Angew. Chemie - Int. Ed.* **56**, 10114 (2017).
- ¹⁸ “Diamond RIXS I21,” .
- ¹⁹ J. Pelliciani, Y. Huang, T. Das, M. Dantz, V. Bisogni, P. O. Velasco, V. N. Strocov, L. Xing, X. Wang, C. Jin, and T. Schmitt, *Phys. Rev. B* **93**, 134515 (2016).
- ²⁰ G. Kresse and J. Furthmüller, *Phys. Rev. B* **54**, 11169 (1996).
- ²¹ J. P. Perdew, K. Burke, and M. Ernzerhof, *Phys. Rev. Lett.* **77**, 3865 (1996).
- ²² P. Fischer, G. Rault, and D. Schwarzenbach, *J. Phys. Chem. Solids* **32**, 1641 (1971).
- ²³ N. Marzari, A. a. Mostofi, J. R. Yates, I. Souza, and D. Vanderbilt, *Rev. Mod. Phys.* **84**, 1419 (2012).
- ²⁴ H. Eskes, L. H. Tjeng, and G. A. Sawatzky, *Phys. Rev. B* **41**, 288 (1990).
- ²⁵ S. Uchida, T. Ido, H. Takagi, T. Arima, Y. Tokura, and S. Tajima, *Phys. Rev. B* **43**, 7942 (1991).
- ²⁶ J. P. Falck, A. Levy, M. A. Kastner, and R. J. Birgeneau, *Phys. Rev. Lett.* **69**, 1109 (1992).
- ²⁷ G. A. Thomas, D. H. Rapkine, S. L. Cooper, S.-W. Cheong, A. S. Cooper, L. F. Schneemeyer, and J. V. Waszczak, *Phys. Rev. B* **45**, 2474 (1992).
- ²⁸ J. P. Falck, J. D. Perkins, A. Levy, M. A. Kastner, J. M. Graybeal, and R. J. Birgeneau, *Phys. Rev. B* **49**, 6246 (1994).
- ²⁹ S. L. Cooper, G. A. Thomas, A. J. Millis, P. E. Sulewski, J. Orenstein, D. H. Rapkine, S.-W. Cheong, and P. L. Trevor, *Phys. Rev. B* **42**, 10785 (1990).
- ³⁰ J. D. Perkins, J. M. Graybeal, M. A. Kastner, R. J. Birgeneau, J. P. Falck, and M. Greven, *Phys. Rev. Lett.* **71**, 1621 (1993).
- ³¹ D. N. Basov and T. Timusk, *Rev. Mod. Phys.* **77**, 721 (2005).
- ³² S. Tajima, *Reports on Progress in Physics* **79**, 094001 (2016).
- ³³ C. T. Chen, F. Sette, Y. Ma, M. S. Hybertsen, E. B. Stechel, W. M. C. Foulkes, M. Schuster, S.-W. Cheong, A. S. Cooper, L. W. Rupp, B. Batlogg, Y. L. Soo, Z. H. Ming, A. Krol, and Y. H. Kao, *Phys. Rev. Lett.* **66**, 104 (1991).
- ³⁴ S. Nakai, A. Kawata, M. Ohashi, M. Kitamura, C. Sugiura, T. Mitsuishi, and H. Maezawa, *Phys. Rev. B* **37**, 10895 (1988).
- ³⁵ P. Olalde-Velasco, J. Jiménez-Mier, J. Denlinger, and W.-L. Yang, *Phys. Rev. B* **87**, 245136 (2013).
- ³⁶ F. Bondino, M. Malvestuto, E. Magnano, M. Zangrando, M. Zacchigna, P. Ghigna, and F. Parmigiani, *Phys. Rev. B* **79**, 115120 (2009).
- ³⁷ V. Bisogni, L. Simonelli, L. J. P. Ament, F. Forte, M. Moretti Sala, M. Minola, S. Huotari, J. van den Brink, G. Ghiringhelli, N. B. Brookes, and L. Braicovich, *Phys. Rev. B* **85**, 214527 (2012).
- ³⁸ C. Friebel and D. Reinen, *Zeitschrift für Anorg. und Allg. Chemie* **413**, 51 (1975).
- ³⁹ A. Monnier, A. Gerber, and H. Bill, *J. Chem. Phys.* **94**, 5891 (1991).
- ⁴⁰ J. A. Aramburu, M. Moreno, and M. T. Barriuso, *J. Phys. Condens. Matter* **4**, 9089 (1992).
- ⁴¹ R. Valiente, J. A. Aramburu, M. T. Barriuso, and M. Moreno, *J. Phys. Condens. Matter* **6**, 4515 (1994).
- ⁴² Z. Mazej, T. Michałowski, E. A. Goreshnik, Z. Jagličić, I. Arčon, J. Szydłowska, and W. Grochala, *Dalt. Trans.* **44**, 10957 (2015).
- ⁴³ L. Hozoi, L. Siurakshina, P. Fulde, and J. Van Den Brink, *Sci. Rep.* **1**, 1 (2011).
- ⁴⁴ M. M. Sala, V. Bisogni, C. Aruta, G. Balestrino, H. Berger, N. B. Brookes, G. M. de Luca, D. D. Castro, M. Grioni, M. Guarise, P. G. Medaglia, F. M. Granozio, M. Minola, P. Perna, M. Radovic, M. Salluzzo, T. Schmitt, K. J. Zhou, L. Braicovich, and G. Ghiringhelli, *New Journal of Physics* **13**, 043026 (2011).
- ⁴⁵ E. Dagotto, *Rev. Mod. Phys.* **66**, 763 (1994), 9311013.
- ⁴⁶ M. W. Haverkort, M. Zwierzycki, and O. K. Andersen, *Phys. Rev. B* **85**, 165113 (2012).
- ⁴⁷ V. Brosco, Z.-J. Ying, and J. Lorenzana, *Sci. Rep.* **3** (2013).
- ⁴⁸ W. Grochala, R. G. Egdell, P. P. Edwards, Z. Mazej, and B. Žemva, *ChemPhysChem* **4**, 997 (2003).
- ⁴⁹ C. Shen, B. Žemva, G. M. Lucier, O. Graudejus, J. A. Allman, and N. Bartlett, *Inorg. Chem.* **38**, 4570 (1999).
- ⁵⁰ J. Romiszewski, W. Grochala, and L. Z. Stolarczyk, *Journal of Physics: Condensed Matter* **19**, 116206 (2007).
- ⁵¹ K. Tokár, M. Derzsi, and W. Grochala, *Computational Materials Science* **188**, 110250 (2021).
- ⁵² C. M. Varma, *Reports Prog. Phys.* **75**, 052501 (2012).
- ⁵³ S. Bandaru, M. Derzsi, A. Grzelak, J. Lorenzana, and W. Grochala, *Phys. Rev. Mater.* **5**, 064801 (2021).
- ⁵⁴ A. Grzelak, H. Su, X. Yang, D. Kurzydłowski, J. Lorenzana, and W. Grochala, *Phys. Rev. Mater.* **4**, 084405 (2020), arXiv:2005.00461.
- ⁵⁵ R. Trębiński, W. A. Trzcieski, and E. Włodarczyk, *J. Techn. Phys.* **27**, 3 (1986).